Dual-Matrix Composite Wideband Antenna Structures for CubeSats

M. Sakovsky,[*] I. Maqueda,[†] C. Karl,[‡] and S. Pellegrino[§]

California Institute of Technology, CA 91125

J. Costantine [¶]

University of New Mexico, NM 87131

Abstract

A concept for a deployable high-performance antenna structure for CubeSats is presented. The detailed design of a conical log-spiral antenna with wideband operation between 250 - 500 MHz, a gain of above 5 dB, and circular polarization is performed using electromagnetic simulations. A structural concept using dual-matrix composites with soft hinge regions, allowing the antenna to be packaged into small volumes, is developed. An antenna prototype is fabricated using Astroquartz fibers, an epoxy matrix, and a high-strain silicone matrix for the hinge regions. Structural and electromagnetic analysis is conducted and shows good agreement with predicted performance thus demonstrating the validity of the proposed antenna concept.

I. Introduction

The tightly constrained volume available in CubeSats limits the capabilities of the payloads and the performance of subsystems such as power and communications. The predominant choices for a CubeSat communications system are dipole or monopole antennas. These types of antennas are easy to stow and are commercially available, but tend to be limited by low efficiency and low gain. To improve bandwidth and efficiency, it is desirable to utilize antenna designs that currently are only present on large satellites, due to their greater size and complexity.

The size of an antenna is inversely proportional to its frequency, which makes packaging a high-gain and high-frequency antenna into a CubeSat challenging. Olson et al.[13] proposed several concepts for deployable wideband antennas compatible with CubeSats and operating in the 250-500 MHz range, covering part of both the Very High Frequency (VHF) and Ultra High Frequency bands (UHF), and with circular polarization. The structural concepts behind these antennas allow them to be stowed in small volumes.

This paper focuses on foldable fiber composite materials, in which the matrix is a soft, high strain elastomer. Such structures have been proposed[3,11] for self-deployable space structures as an alternative to mechanical hinges or thin-walled shell elements. Composite materials with a high-strain elastomer can be folded into very high curvatures without suffering significant damage, as the fibers in the compression side of the fold undergo microbuckling, preventing them from breaking.[1,8,12]

Many self-deployable structures require stiff components for structural reasons or for storing enough strain energy during stowage in order to deploy in space. For this reason, structures entirely made of soft matrix composites are not adequate for some applications. This issue is addressed by designing and building

---

[*]Graduate Student, Graduate Aerospace Laboratories, 1200 East California Boulevard, Mail Code 105-50. e-mail: msakovsk@caltech.edu

[†]Ph.D., Graduate Aerospace Laboratories, 1200 East California Boulevard, Mail Code 105-50. e-mail: imaqueda@caltech.edu

[‡]Visiting Student Researcher from Technical University of Munich. e-mail: christophkarl89@gmail.com

[§]Professor of Aeronautics and Civil Engineering, Graduate Aerospace Laboratories, 1200 East California Boulevard, Mail Code 301-46, Fellow AIAA. e-mail: sergiop@caltech.edu

[¶]Research Associate Professor, Electrical and Computer Engineering Department, Albuquerque, NM. e-mail: jcostantine@ieee.org

American Institute of Aeronautics and Astronautics

continuous thin composite shells with localized soft regions. This concept, called dual-matrix composites, was first addressed in[10] .

This paper aims to study the design of a conical log-spiral antenna supported by a dual-matrix composite shell structure. Many challenges need to be addressed to design this type of structure. Section II discusses the selection of the log-spiral antenna and dual-matrix composites as a way to satisfy antenna electromagnetic and structural requirements. Section III discusses material selection and testing. In Section IV, a detailed electromagnetic and structural analysis of a particular antenna geometry will be conducted. Section V, explains the fabrication process of a prototype with this geometry. Finally, Sections VI and VII detail the testing conducted on the fabricated prototype to verify its expected performance. It is demonstrated that a conical log-spiral antenna supported by a dual-matrix composite shell is a design that can satisfy both the electromagnetic and structural requirements and hence is suitable for use as efficient antennas for CubeSats.

II.   Antenna Concept

A 6U CubeSat mission has been proposed in which a high performance antenna would need to be packaged in a volume no larger than $20 \times 10 \times 5$ cm (half of a 2U CubeSat). The antenna is to have gain of at least 5 dB, wideband operation in the UHF band (250 - 500 MHz), and exhibit circular polarization. Structurally, the antenna must be low cost, lightweight, simple, and robust. This section explores several antenna architectures and structural concepts to identify a candidate solution.

II.A.   Antenna Architectures

Although several antenna architectures can meet the above requirements, the quadrifilar helix and conical log spiral antennas are the best fit. This is due to their natural circular polarization and high gain characteristics. The design and modeling of antenna architectures and performance was done using electromagnetic and structural numerical simulators.
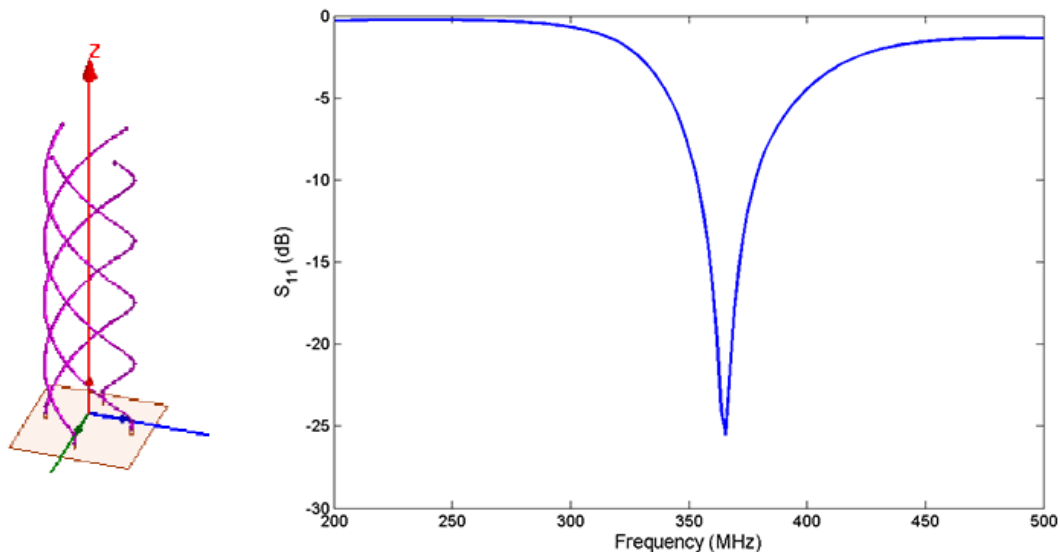

Figure 1. Quadrifilar antenna and reflection coefficient measurements (The required is defined for $S_{11} <$ -10 dB).

A quadrifilar helix antenna consists of four helical conductor arms rotated 90° with respect to each other around a central axis, see Figure 1. The antenna is circularly polarized, omni-directional, and can meet the gain requirements. However, the antenna exhibits narrow band behaviour as shown in the reflection coefficient plot in Figure 1. Thus, it is concluded that a quadrifilar helix antenna in its conventional topology cannot cover the entire needed bandwidth. A solution for this problem may be to design a quadrifilar antenna with different arm lengths. Good bandwidth coverage can be achieved as shown in Figure 2. However, it is important to indicate that this topology does not exhibit the same high gain as the conventional design and requires robust decoupling between the various antenna arms to preserve the coverage of the active reflection

American Institute of Aeronautics and Astronautics
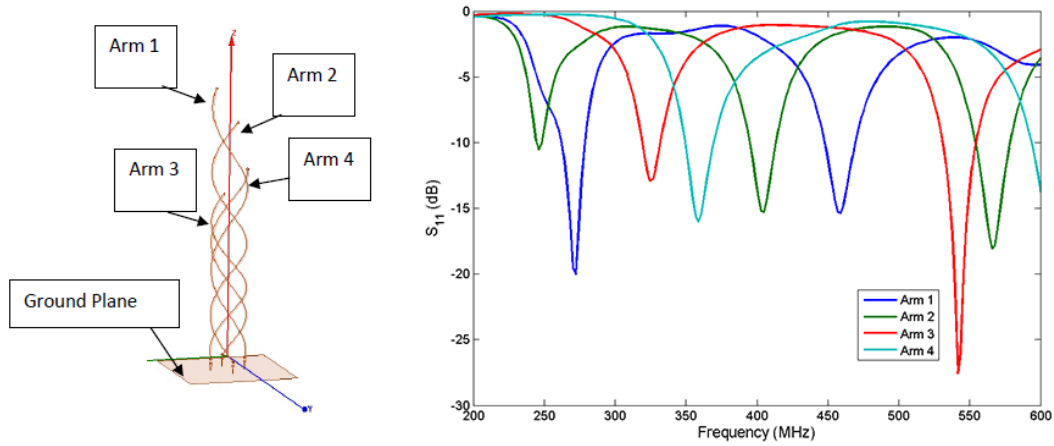
coefficient.

Figure 2. Quadrifilar antenna with four different arm lengths and reflection coefficient for each arm (The required bandwidth is defined for $S_{11} <$ -10 dB).

An alternative antenna architecture is the conical log spiral antenna composed of two strips of conductor, with its dimensions varying log-periodically with the conductor length, wound around the face of a cone, as shown in Figure 3. This antenna also exhibits circular polarization and can meet the gain requirements, however its logarithmic periodicity forces its radiation pattern to be directed towards the apex of the cone. It is important to note that his antenna is typically fed at the top of the cone. Reflection coefficient simulations show that it is possible to achieve wideband operation covering the entire desired bandwidth of 250 - 500 MHz, Figure 3. The feeding position at the top of the apex may cause some difficulties in the deployment mechanisms and thus it may be beneficial to investigate an alternative feeding technique. Optimization of the feeding position has resulted in the conclusion that this antenna can also be fed at the bottom over an optimized ground plane. Such feeding position allows the antenna to have the same radiation characteristics as the one fed at the top, however the deployment of a ground plane will be required in this case.
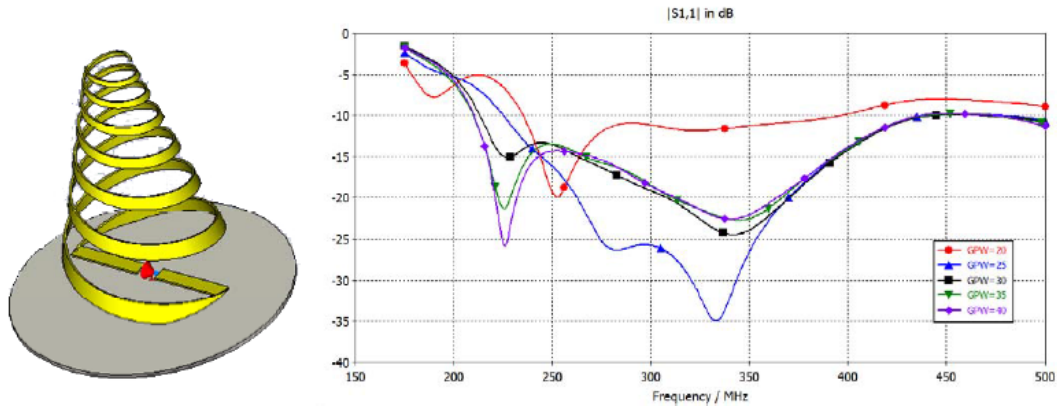

Figure 3. Conic log spiral antenna and reflection coefficient measurements with varying ground plane radii (The bandwidth is defined for $S_{11} <$ -10 dB).

Although both antennas could meet the circular polarization and gain requirements for the antenna, it was found that the conical log spiral antenna satisfies the bandwidth requirements more efficiently.

II.B. Structural Concepts

Several concepts for deployable antennas that satisfy the stated requirements have been proposed in Olson et al.[13] These schemes fall under two categories: helical pantographs and thin shells structures. Both concepts

American Institute of Aeronautics and Astronautics

use strain energy to deploy, thus greatly simplifying and reducing the weight of the deployment mechanisms required.

Standard pantographs consist of pairs of straight rods connected by scissor joints, and attached by revolute joints. This concept has been extended to curved rods to create helical pantographs. The scissor joints allow the helix to be flattened axially. However, this increases the diameter and hence further compaction needs to be achieved by folding the helical arms transversely, Figure 4. The conductors can be added along the cone defined by the support rods. Finite element simulations revealed that the axial force and circumferential torque required for the folding vary monotonically, indicating that the deployment can be controlled using a single constraint. A disadvantage of this structural scheme is the large number of rods and mechanical joints required making it structurally complex. Its complexity would be further increased to accommodate the varying arm lengths required to achieve the desired wideband operation.
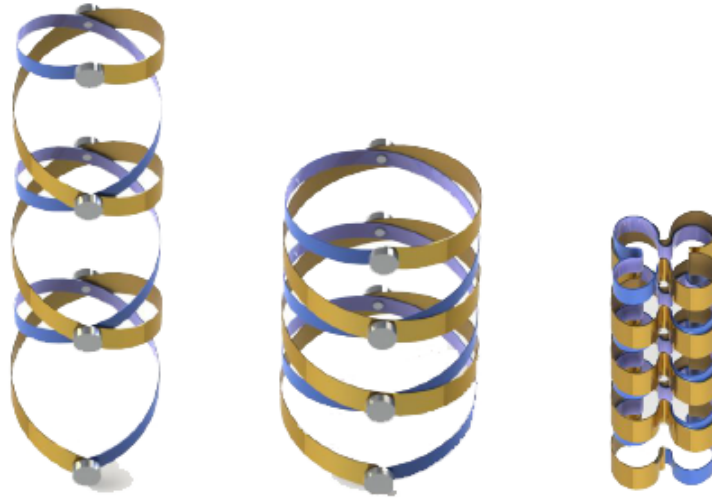

Figure 4. Folding of a helical pantograph.

A second structural concept is that of a thin composite shell that has continuous fibers embedded in a high-strain soft matrix on specific hinge lines and a traditional stiff matrix elsewhere, allowing the shell to fold along the hinge lines. Plastic deformation and damage to the composite due to high curvature at the hinges is prevented by fiber microbuckling.[9] This mechanism prevents the yield strain of the fibers being reached. The conducting elements can be embedded in the composite shell, in between the laminate layers, and do not interfere with the shell folding due to their small thickness.

A dual-matrix antenna can achieve large compaction ratios. It is folded in two steps: the antenna is flattened and the resulting planar structure is folded further. Simple z-folding can be used for the second step where no axial compaction is required, see Figure 5, or the more efficient Miura-ori folding pattern can be used if higher packaging ratios are required.

The use of thin shells eliminates the need for mechanical joints, greatly reducing the complexity of these structures. Furthermore, thin shell structures are more easily adaptable to various antenna architectures. However, a concern that arises with the use of soft matrix materials is the overall stiffness of the structure. This issue will be addressed in Section IV.

II.C. Selected Concept

In order to meet both the antenna performance and the structural requirements specified above, a conical log-spiral antenna was chosen. A prototype will be fabricated with the use of a conical composite shell. The remainder of the paper will discuss the design, analysis, fabrication, and testing of a prototype with z-folding only. Once characterization of the antenna has been completed, the entire concept can be extended to larger antennas requiring the Miura-ori folding scheme.
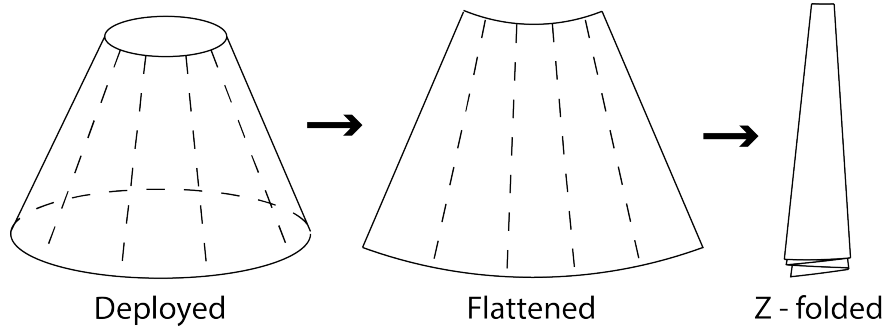
American Institute of Aeronautics and Astronautics

Figure 5. Folding of thin composite shells where the dashed lines indicate the soft matrix hinges.

III.   Materials

Shell and conductor materials are selected and their compatibility discussed prior to a more detailed analysis of the entire structure.

III.A.   Structural Materials

Dual-matrix composite structures described in literature[14, 16] require the use of a woven carbon fiber cloth, heat-cure silicone rubber, and an epoxy matrix. Heat-cure silicones with the desired properties are commercially available, and many of them are outgassing approved for space applications. However, there are several problems related to the use of heat-cure silicones for dual-matrix applications. Heat-cure silicones have a long and non-uniform curing process resulting in bubble formation in hinge regions and flow of silicone into the epoxy matrix regions. In addition, attempts to use heat-cure silicone in the laboratory presented cure inhibition likely due to the presence of epoxy. These factors make it difficult to obtain the desired material properties in and around the silicone hinge areas.

The final approach that was developed to address these issues was to use an ultraviolet (UV)-cure silicone (a heat-cure process was also developed, see Section V.A for details). UV curing is a photochemical process in which UV radiation is used to initiate the catalytic curing reaction. As the silicone is UV-transparent, the degree of cure through the thickness is uniform. The UV exposure time of these types of silicones can be as low as 0.5 seconds, and the curing can be performed at low temperatures. Due to the fast curing time, the flow of the silicone towards undesired regions before curing is minimized. Additionally, the quick surface cure does not trap voids within the laminate. UV cure silicones are not as sensitive to other chemicals as heat-cure silicones, presenting less or no inhibition to cure.

Consideration was required for appropriate fiber selection. UV energy can only penetrate optically transparent material, so it cannot be used with carbon fibers unless each ply is cured separately. While fiberglass is optically transparent, UV energy will not penetrate farther than 13 to 19 mm into the material, requiring thicker laminates to be cured separately as well. Furthermore, a fabric with high out-of-plane stiffness is desired to minimize the number of plies in the composite to aid in better folding of the shell.

With these considerations, the materials that were used for the dual-matrix prototypes are fiberglass, epoxy and UV-cure silicone.

- Epoxy: the Hexply ® 913 epoxy resin delivered in film form on a paper backing. Once the film is heated, the resin is transfered to the dry fabric. The advantage of using epoxy film over liquid epoxy or pre-impregnated fabric is that the film can be cut in different shapes, allowing a good definition of the geometry of the folding area.

- Silicone: The UV-curing silicone LOCTITE® 5055 ™[7] has been selected due to its viscosity in an uncured state, which is low enough to spread through the thickness of the glass fabric, and high enough that the fibers can be impregnated in a controlled way. LOCTITE® 5055 ™ is an alkoxy silicone, which comes in a single liquid component. The silicone cures up to a depth time of 4 mm in 60 seconds, with a UV radiation of 70 mW/cm^2 and a wavelength of 365 nm.

- Fiberglass: Astroquartz® II 525 plain weave fabric from JPS composites has been chosen. Astroquartz®

American Institute of Aeronautics and Astronautics

II fibers are high-strength fibers with a 99.99% silica content. This material is used in applications requiring low dielectric loss, such as antennas.

The properties provided by the manufacturers are given in Table 1.

Material	ρ (g/cm^{-3})	E (GPa)	Tensile Strength (MPa)
Epoxy	1.23	3.39	65.5
Silicone	0.98	0.002	9.3
Astroquartz®	2.2	72	6000

Table 1. Properties of silicone, epoxy, and Astroquartz® (provided by the suppliers). ρ is the density and E the elastic modulus.

III.B.   Electric Conductor

The conductor needs to be thin to minimize its effect on the folding capabilities of the dual-matrix shell. Additionally, the thickness needs to be greater than 2δ, where δ is the skin depth of the metal at the lowest operating frequency (250 MHz). The skin depth is inversely proportional to the frequency, f, and depends on the conductor resistivity and relative permeability, ρ and μ_R, respectively:

$$\delta = \sqrt{\frac{\rho}{\pi f \mu_0 \mu_R}}, \tag{1}$$

where $\mu_0 = 4\pi \cdot 10^{-7}$ Vs/Am is the permeability of the vacuum.

Thin conductor sheets can reach high curvatures, but may break when folded into sharp kinks. Another option is printing the metallic conductor on the laminate, during or after the fabrication of the laminate. Conductive metallic tapes may be used as well.

The conductor used here is a phosphor bronze woven mesh from TPW Inc., with 325 wires per inch and a wire diameter of 28 μm, Figure 6. Phosphor bronze is an alloy of 94.8% copper, 5% tin and 0.2% phosphorous. This material has good physical properties, fair electrical conductivity and moderate cost. The skin depth of bronze at 250 MHz, defined from Equation 1, is $\delta \sim 6$ μm. The wire diameter is larger than δ, making this material suitable for the antenna application.

The advantage of using a wire mesh instead of solid conductor strips is that it can be folded into very sharp kinks. Although, the mesh shows a distortion, no breaks are seen as the ultimate strain is not attained. The low stiffness of the mesh minimizes its effect on the folding capabilities of the composite laminate. Additionally, electromagnetic tests conducted before and after folding show little change in radiation behaviour.

The conductor is integrated in the dual-matrix shell by embedding it in the laminate mid-plane. The mesh allows the UV light to penetrate enough so that the silicone is well cured through the thickness of the laminate. Figure 7 shows schematically how the conductor is embedded in the composite.
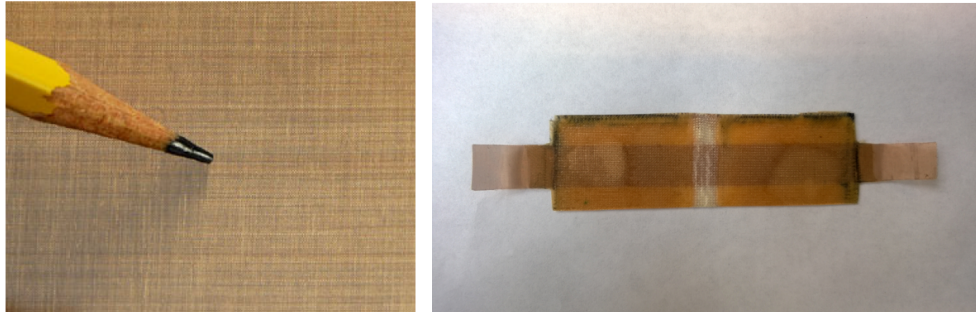

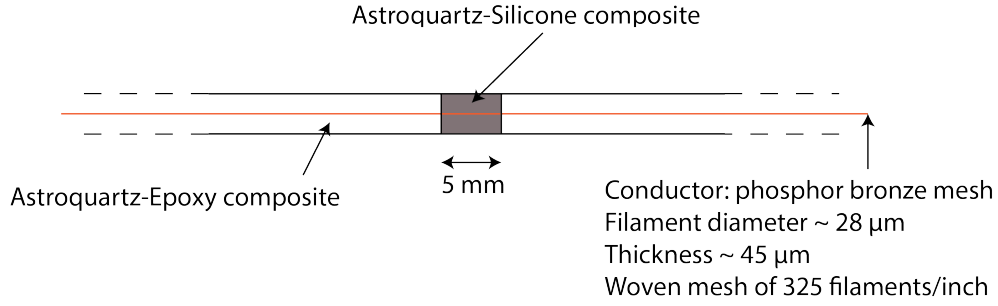**Figure 6. Phosphor bronze conductive mesh (left) and conductor embedded in a dual-matrix laminate (right).**

American Institute of Aeronautics and Astronautics

Figure 7. Thickness view of composite laminate, showing silicone region and conductor.

III.C.   Prototypes

Flat plate prototypes were fabricated using these materials to verify the validity of the dual-matrix concept and characterize matrix mixing. The hinges were 160 mm long with a width of 25 mm and a 5 mm wide hinge region. A quasi-isotropic $[\pm 30, 0]_s$ layup was used. Figure 8 shows the hinge deployed as well as in a folded configuration of 180°. Thickness measurements of the prototypes show 387 μm thick epoxy panels and 413 μm thick silicone hinges, on average.
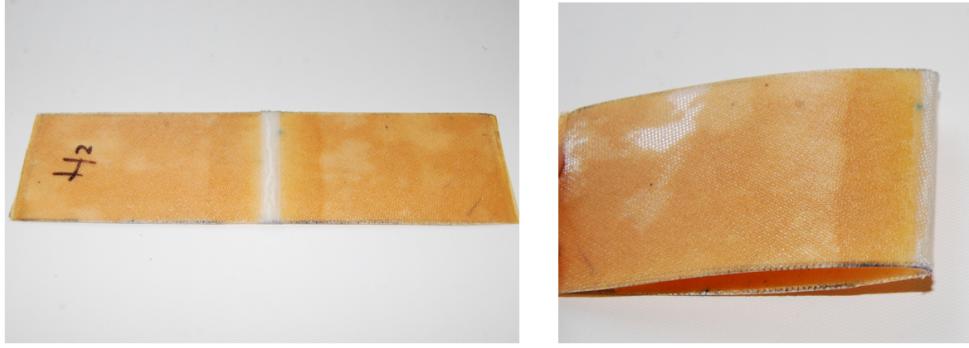

Figure 8. Astroquartz dual-matrix laminate with silicone hinge, unfolded and folded.

Figure 9 is a micrograph of the hinge interface region taken with a Nikon Eclipse LV150N microscope at 10× magnification. The image shows a small, non-planar interface region approximately 0.5 mm wide. Nanoindentation was used to characterize the mechanical properties of the two matrices close to the interface region. The tests were conducted using a Hysitron T1950 Triboindenter with a Berkovich tip. Nanoindentation tests require a surface finish at least an order of magnitude less than the indent depth of 1 μm. Hence, the samples were potted in epoxy and polished with successively finer compounds up to a final polish with the 0.05μm Buehler Micropolish Alumina suspension. Scanning probe microscopy using the T1950 Triboindenter showed a surface finish of at most 0.6 nm rms.

The samples were loaded at a rate of 33.3 nm/s up to an indent depth of 1 μm, held for 2 mins, and unloaded at the same rate. The load and indent depth were measured using a three-plate capacitive transducer. The modulus of the material was then deduced from:[6]

$$E_r = \frac{dP}{dh} \frac{1}{2\beta} \sqrt{\frac{\pi}{A}}$$

$$\frac{1}{E_r} = \frac{1 - \nu^2}{E} + \frac{1 - \nu_i^2}{E_i}$$

where $\frac{dP}{dh}$ is the load vs. indent depth slope at unloading, β is a geometric factor calculated from finite element simulations, A is the indenter area, E_r is the reduced modulus, and i indicates the indenter properties. The area of the indenter was calibrated by indenting into a fused silica sample with known properties.

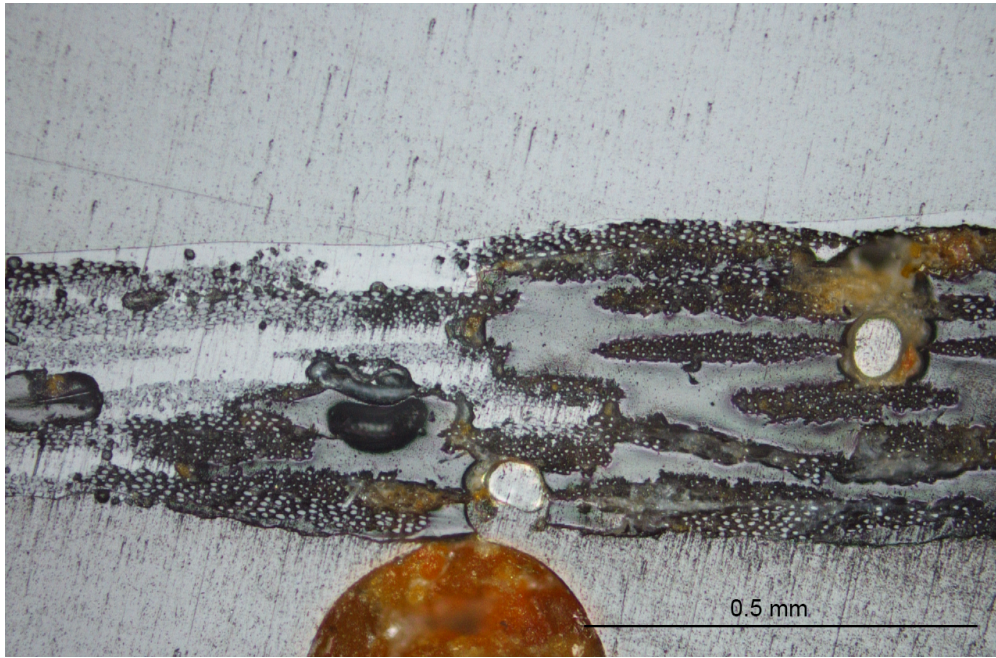American Institute of Aeronautics and Astronautics

Figure 9. Micrograph of matrix interface region.

Table 2 shows the epoxy and silicone moduli as a function of distance from the interface. Modulus values for both matrices show reasonable agreement with the values in Table 1. It can be seen that there is a slight softening of the epoxy modulus closer to the matrix interface, followed by a sharp drop across the interface. Silicone measurements were only taken close to the interface due to the significant noise and inaccuracies associated with indenting a soft matrix.

Distance from Interface	5mm	2mm	30 μm
Epoxy Modulus (GPa)	3.74	3.49	3.30
Silicone Modulus (MPa)	-	-	14.2

Table 2. Matrix modulus values from nanoindentation tests.

Nanoindentation showed that matrix mixing has been limited by the use of UV-cure silicone and no significant softening of the epoxy panels or stiffening of the silicone hinges occurs for this selection of materials. The interface region is confined to the 0.5 mm non-planar region seen in Figure 9. Hence, this choice of materials allows for fabrication of structures with well-defined hinge geometries and will be used for manufacturing of a full prototype.

IV. Design and Analysis

Having chosen a specific antenna concept and selected the materials for a prototype, the antenna dimensions that allow the design to meet all performance requirements have to be selected. This was done through a combination of electromagnetic simulations and structural analysis. The electromagnetic simulations allow optimization of the antenna geometry to attain the best electromagnetic performance. A structural analysis of the selected geometry was done for a full characterization of the antenna to verify the feasibility of the concept.

IV.A. EM Design parameters

Electromagnetic simulations were performed in order to determine the precise dimensions of the antenna and conductor. The effects of changing the antenna geometry (defined by: the generator length, expansion coefficient, the upper and lower radii, and antenna height) on the antenna gain, polarization, operating

frequencies, and radiation pattern were investigated.

Many general guidelines for the design of conical log spiral antennas exist. For example, Dyson notes that the propagating frequency is dependent on the ratio between the outer and inner radii of the antenna.[4] The larger the ratio, the better the performance of the antenna is at lower frequencies. Additionally, a tightly wound antenna, i.e. an antenna with a smaller expansion coefficient, can help the directivity at the expense of antenna performance as this will decrease the ratio of the outer to inner radius.

Optimization over these parameters is complex and hence the generator length of the antenna was selected as a metric for determining the performance of the antenna. In the design of a conical log spiral antenna, the cone generator length depends on three structural parameters: the vertical height of the antenna, the inner radius (at the top of the antenna), and the expansion coefficient which represents the shape and topology of the cone and how it is expanded. It is important to note that the outer radius of the cone is a function of the inner radius due to the logarithmic distribution of the conductor. The upper limit for the generator length was taken to be equal to 19.6 cm. The variation of any of the antenna geometrical parameters results in a change in performance even if the cone generator length is preserved.

The chosen antenna dimensions that exhibit the most suitable electromagnetic behaviour and structural performance are shown in Table 3. The predicted antenna performance for this geometry can be seen in Figure 10.

From the antenna's reflection coefficient shown in Figure 10a is can be determined that the antenna's expected operating frequency varies from 318 to 600 MHz. The antenna exhibits a major lobe radiation towards the apex of the cone with a gain above 5 dB and a minimum back lobe radiation, as shown in Figure 10b for a radiation pattern at 400 MHz. The antenna is also naturally circularly polarized due to its helical topology.

Cone Generator	19.6 cm
Inner Radius	7.0 cm
Outer Radius	14.1 cm
Number of Conductor Turns	1.25
Expansion Coefficient	1.75
Cone Height	18.5 cm

Table 3. Antenna prototype geometry

The length of the generator of the truncated cone is 19.6 cm, which is smaller than the longest dimension of the available space in the CubeSat. Therefore, this antenna design can be packaged by flattening the cone and z-folding the flattened shell into trapezoidal panels, as shown in Figure 5. The prototype cone is divided into 12 hinges resulting in the geometry as shown in Figure 11.

IV.B. Mechanical Properties

For simplicity, a quasi-isotropic composite layup was selected. In plain-weave fabric, warp and weft tows are woven perpendicularly. Hence, taking the angle of one of the woven tows as a reference, a possible quasi-isotropic symmetric laminate could be $[0/45]_s$, where s indicates a symmetric laminate. This laminate is a 4-ply plain weave that presents tows at every 45°. However, samples made in the laboratory with this configuration were not sufficiently stiff, so a thicker laminate was required.

The laminate $[\pm30/0]_s$ is also quasi-isotropic, as it is composed of 6 plain weave laminas that have tows at every 30°, (Figure 12). Samples with this configuration were stiff enough, and sufficient strain energy was stored at a fold that the deployment was autonomous.

IV.B.1. Estimation of shell mechanical properties

Classical Laminate Theory (CLT) was used to estimate the mechanical properties of the composite. The homogenized properties of each unidirectional ply (E_1, E_2, ν_{12}, G_{12}) were found from the rule of mixtures and the Halpin-Tsai relation, using the constituent mechanical properties and volume fractions. In the case of woven composites, studying the microstructure of the material to estimate the fiber volume fraction is not trivial, as the voids between warp and weft are filled with extra resin. For this reason, the dry fabric

American Institute of Aeronautics and Astronautics
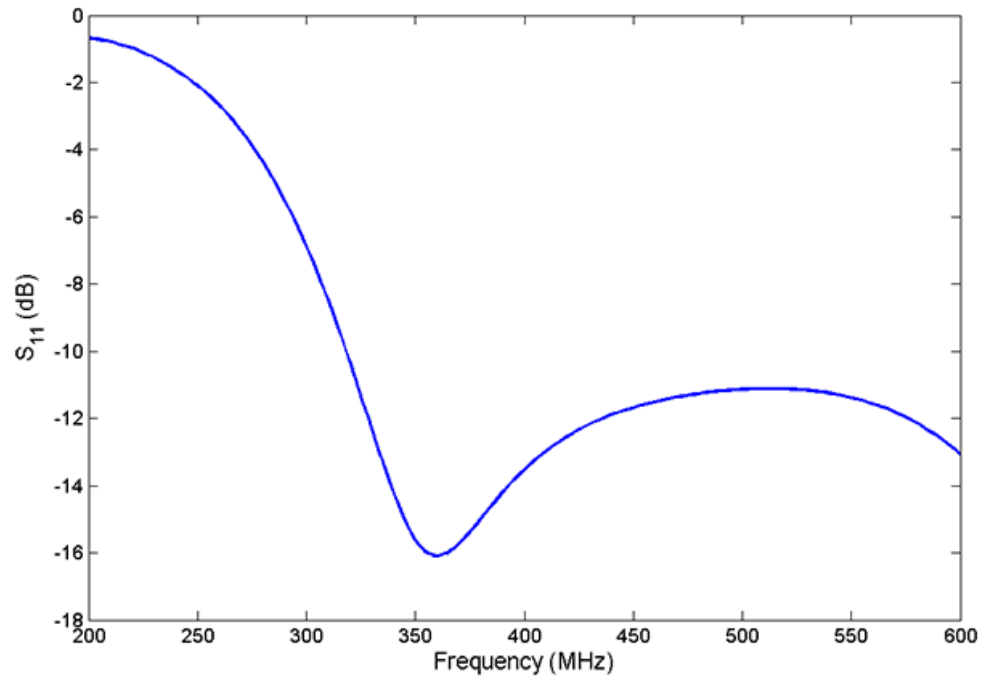
(a)
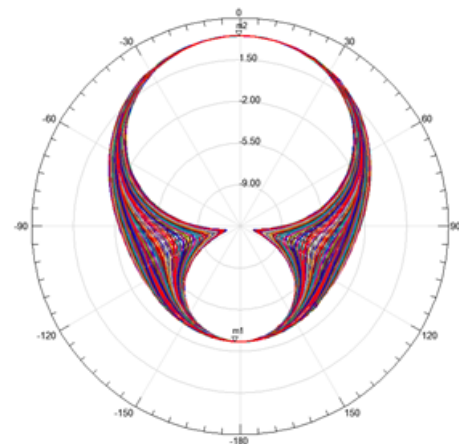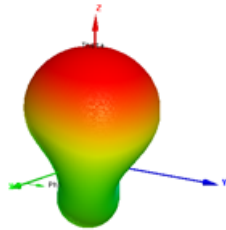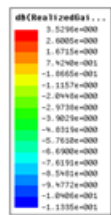
(b)

Figure 10. Electromagnetic performance for selected antenna dimensions. (a) reflection coefficient (b) axial ratio at 400 MHz (c) radiation pattern at 400 MHz
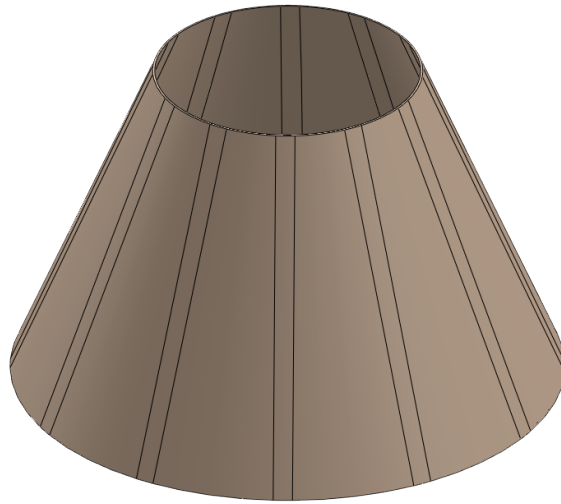
American Institute of Aeronautics and Astronautics

Figure 11. CAD model of finalized antenna geometry.
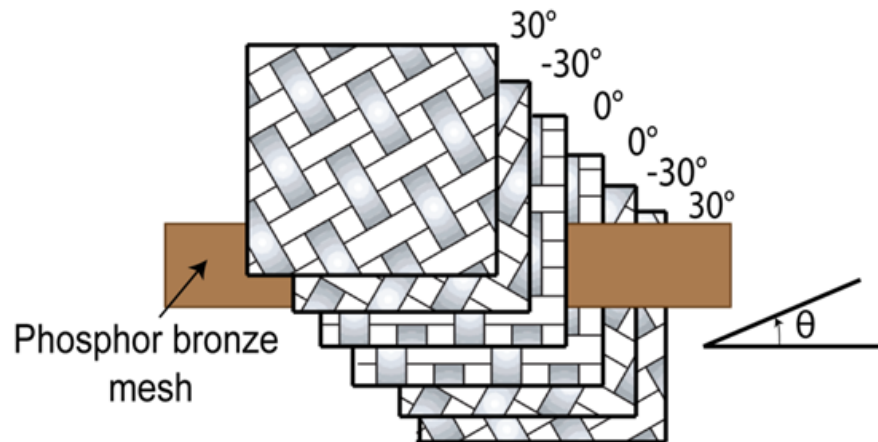
Figure 12. Lay-up of $[\pm 30/0]_s$ plain weave laminate showing the conductor at mid-plane.

American Institute of Aeronautics and Astronautics

and the final composite were weighed with an Acculab® VI precision scale. The resulting fiber fractions are $V_{f,e} = 59\%$ for the epoxy-Astroquartz laminate, and $V_{f,s} = 33\%$ for the silicone embedded hinges. The fiber volume fraction is lower at the hinges because the curing of the silicone is not done in vacuum.

The homogenized ply properties and fiber angles were then used to compute the stiffness matrix, Q, for each ply. The ABD matrix for both epoxy and silicone matrices were calculated from CLT in order to relate applied forces and moments to resulting strains and curvatures in the laminate. CLT is a standard technique for the estimation of laminate properties, more details can be found in Ref.[2]

For woven composites, the in-plane properties can be calculated with good accuracy using CLT. However, this is not the case for the out-of-plane properties. To address this problem, the periodic unit cell representing the weave can be homogenized through finite element models; Soykasap found that CLT predictions are in agreement with more accurate finite element models when the laminates have three or more plies.[15] Soykasap proposed a mosaic model that assumes that each plain weave lamina is divided into subcells occupied by infiltrated yarns.[15] A unit cell of a single plain weave lamina is represented by a 4×4 mosaic model. Each unit cell consists of asymmetrical cross-ply laminates, ignoring the continuity and undulation of the fibers.
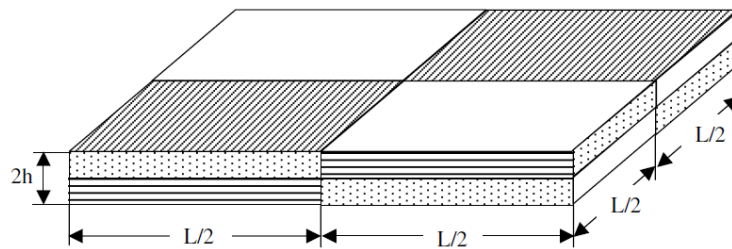

Figure 13. Unit cell of mosaic model, taken from Soykasap.[15]

With this model, the chosen 6-ply plain weave laminate $[\pm 30/0]_s$ can be calculated as if it were composed of 12 laminas, each of which has a stiffness of

$$Q = 0.5(Q_\parallel + Q_\perp). \tag{2}$$

For example, the first lamina is a plain weave with one of the fiber directions at an angle of 30° from the reference axis. The first and second equivalent unidirectional laminas would have an effective stiffness

$$Q = 0.5(Q_{30} + Q_{-60}). \tag{3}$$

This model has been used to calculate the extensional and bending stiffness matrix of the Astroquartz-reinforced epoxy and the Astroquartz-reinforced silicone. $B = 0$ due to the symmetry of the laminate. The thickness of manufactured samples was measured to be $t = 0.35$ mm for the epoxy part of the shell and $t = 0.5$ mm for the silicone. The computed out-of-plane bending stiffness, $D_{11} = D_{22}$ was:

$$D_{11,epoxy} = 93Nmm \tag{4}$$

$$D_{11,silicone} = 79.1Nmm \tag{5}$$

The behavior of both laminates is isotropic and fiber-dominated. The in-plane stiffness of the silicone laminate is about one half the stiffness the epoxy laminate, while the out-of-plane stiffness of the silicone laminate is comparable to the out-of-plane stiffness of the epoxy laminate. This is due to the greater thickness of the silicone laminate.

IV.B.2.   Experimental characterization of fold region

The most probable source of error of the analytical model of the composite is the out-of-plane stiffness. To validate the results, bending tests were performed on full epoxy laminates. Bending tests on laminates with a central silicone hinge (Figure 8) were carried out as well.

The experimental setup is shown in Figures 14. In these experiments, $h = s = 25$ mm. The geometry of the hinges is shown in Figure 15. The full epoxy laminates are similar to these but without the hinge region.
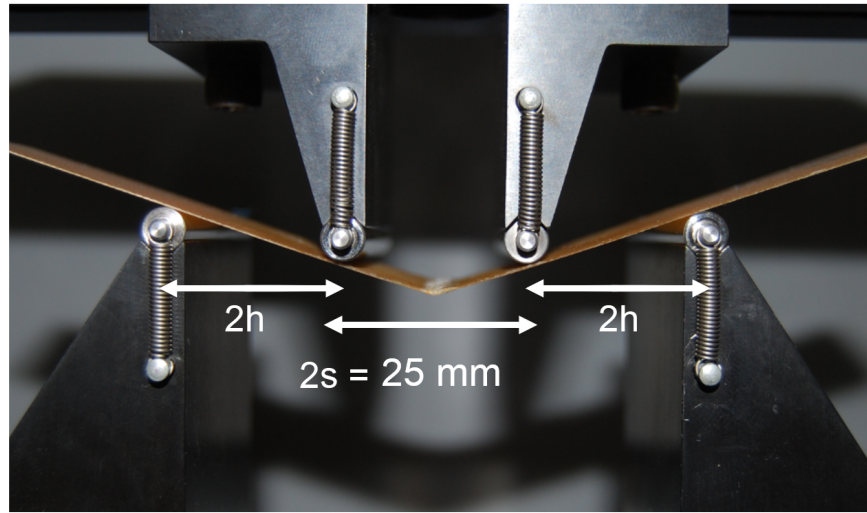
Figure 14. Four-point bending test setup.

The vertical deflection of the center of the samples was measured with a laser extensometer. The load was measured with the 50 N load cell in an Instron 5569.

Figure 16 shows the dependence of the moment on the change of curvature of the shell. The stiff epoxy samples bent elastically, and the linear slope of the plots provides the out-of-plane stiffness $D_{11} = D_{22}$. The initial nonlinearity of the plots is thought to be a result of fiber misalignment, which caused stiffness coupling ($B \neq 0$). The stiffness coupling causes some initial out-of-flatness on some samples, which can explain the initial non-linearity in the plot.
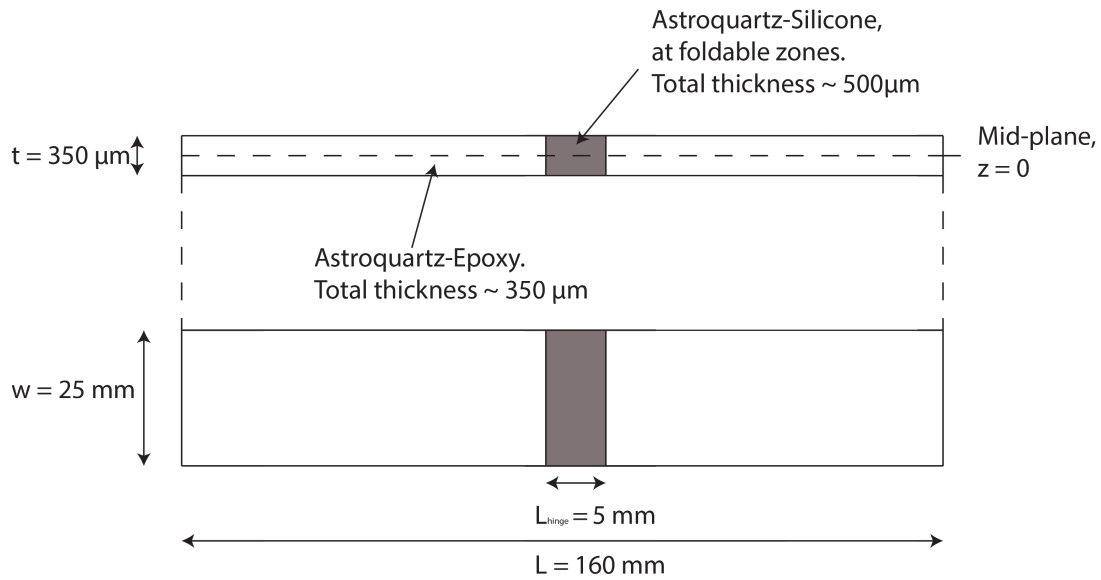

Figure 15. Schematic of the hinge samples manufactured in the laboratory. The laminate is the $[\pm 30, 0]_s$ plain weave laminate studied in the previous section, cured with silicone matrix in the hinge area (in grey), and with epoxy in the rest of the sample.

The average slope of the linear regions of the plot gives $D_{11} \approx 110$ Nmm, which is in relatively good agreement with the prediction $D_{11} = 93$ Nmm.

Finally, four-point bending tests were performed on the hinge samples, see Figure 15. Figure 17 shows the comparison of the behavior of an epoxy laminate sample, a hinge sample before being folded, and the same sample after being folded.

Before being folded, the hinge samples have a stiffness $D_{11} \approx 98$ Nm, higher than the predicted $D_{11} = 79$

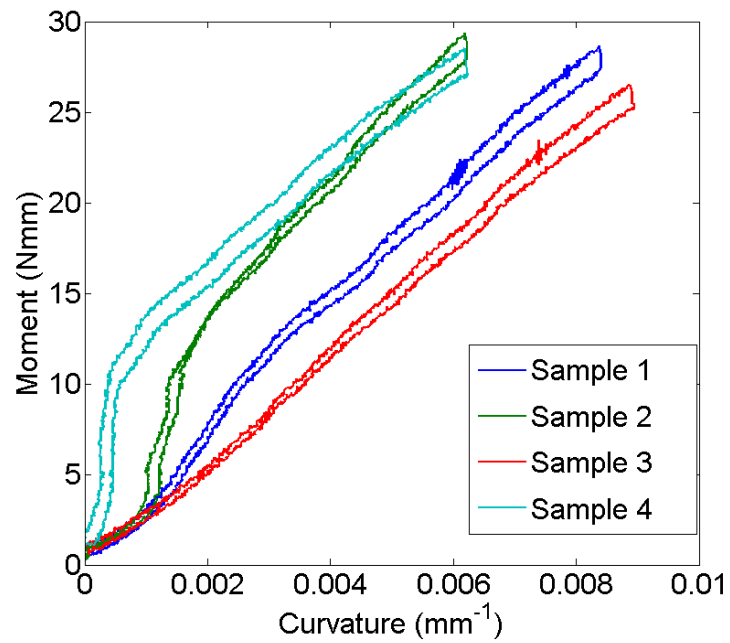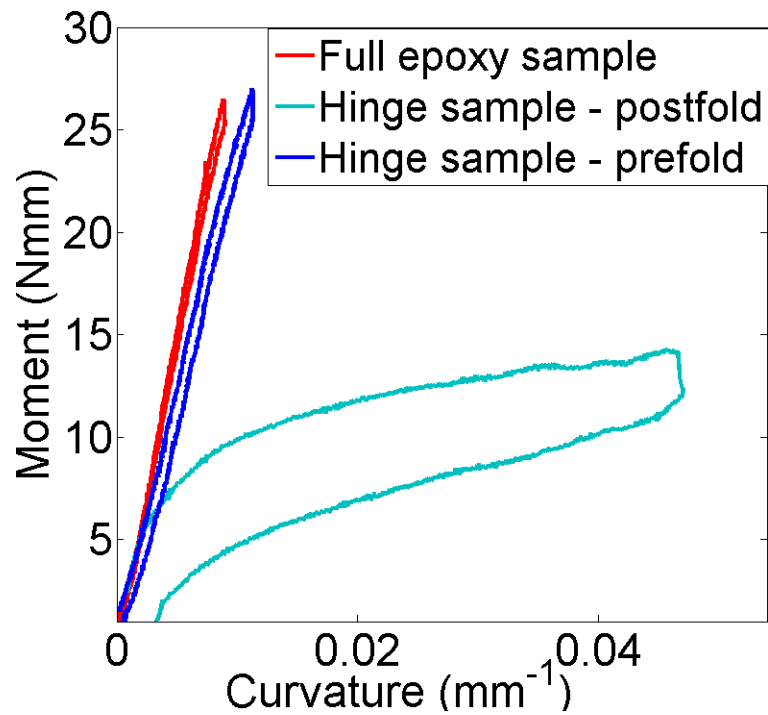American Institute of Aeronautics and Astronautics

Figure 16. Bending tests of AQ-epoxy samples.

Figure 17. Bending tests of one AQ-epoxy sample and one hinge sample, before and after being manually folded.

American Institute of Aeronautics and Astronautics

Nm. The hinge was then folded 180°. The folding was done manually, imposing a curvature radius at the fold of ~ 2 mm. After being folded, the hinge clearly showed a decrease in bending stiffness. The initial stiffness, before the moment reaches 5 Nmm, is the same as before folding. For moments higher than 5Nmm, the hinge starts softening until it approximates to a new linear behavior, with tangent stiffness of ~ 9Nmm. The behavior also presents some hysteresis.

The moment at which the stiffness of the hinge starts decreasing is believed to correspond to the onset of microbuckling in one of the laminas. After this point, and for higher values of the bending curvature, post-microbuckling behavior was observed. Small residual waviness of the fiber was observed after folding and releasing the hinge.

The reduction of the hinge stiffness measured here will be considered when conducting structural simulations of the antenna, in the next section.

IV.C. Vibration analysis

One of the first steps of spacecraft structural design is to investigate the natural frequencies of vibration of the structure to ensure that the natural modes of vibration are away from environmental forcing frequencies.

The natural frequencies of the antenna have been calculated using ABAQUS/Standard with free boundary conditions. The material models of the stiff epoxy panels and the crease lines are calculated using the mosaic model introduced in Section IV.B. However, if the antenna is assumed to have been folded and deployed, the out-of-plane stiffness is reduced. This reduction is considered here, although the experiments showed an initial linear behavior of the after-fold hinge that matched the linear behavior of the stiff laminate. In this model, the out-of-plane bending stiffness D is 10% of the pre-folded stiffness, using a similar value to the stiffness found in the experiments. As a limit case, a bending stiffness of 1% of the pre-folded stiffness has been analyzed. The effect of the conductor has not been taken into account for this analysis.

IV.C.1. Model description

The model was formed with quadrilateral shell elements with reduced integration (S4R). The mesh size was ~ 5 mm in most of the model, except in crease regions where a size of ~ 1 mm was used. The total number of finite elements in the model of the antenna was 18901.

The linear material model was implemented through the ABAQUS command *SHELL GENERAL SECTION for both epoxy and silicone regions. The ABD matrices for the epoxy shell and silicone matrix shells were calculated for the actual thicknesses measured on a sample shell. Average thicknesses of 377 μm for the epoxy and 413 μm for the silicone hinges regions were measured. Furthermore, no thickness was assigned to the shell elements but an areal density was assigned to each section to account for the thickness and to model an antenna with the correct mass distribution.

The eigenfrequencies were obtained with the ABAQUS perturbation analysis module. A total of 10 natural frequencies and modes were obtained for both antenna designs, where the first 6 frequencies correspond to the 6 rigid body nodes in 3D.

IV.C.2. Analysis and results

Table 4 summarizes the results of the eigenfrequency simulations. The frequencies shown are the first, second and third eigenfrequencies for the antenna. Results are given for the unfolded hinges, as well as for hinge out-of-plane stiffness of 10% and 1% of the original, $D_{creases} = 0.1 D_{silicone}$ or $D_{creases} = 0.01 D_{silicone}$. The corresponding modes for 100% and 10% reduced stiffness are shown in Figure 19.

	f_1 (Hz)	f_2 (Hz)	f_3 (Hz)
Unfolded	11.54	12.09	29.73
10% stiffness	6.54	6.77	17.84
1% stiffness	2.35	2.43	6.51

Table 4. **First three natural frequencies of the conical shells, for different values of the out-of-plane stiffness of the hinges.**

Simulations show that the antenna has a higher natural frequency than the standard required value of $f \sim 1$ Hz. With a hinge stiffness of 10% of the pre-fold stiffness, which agrees with the bending experiments
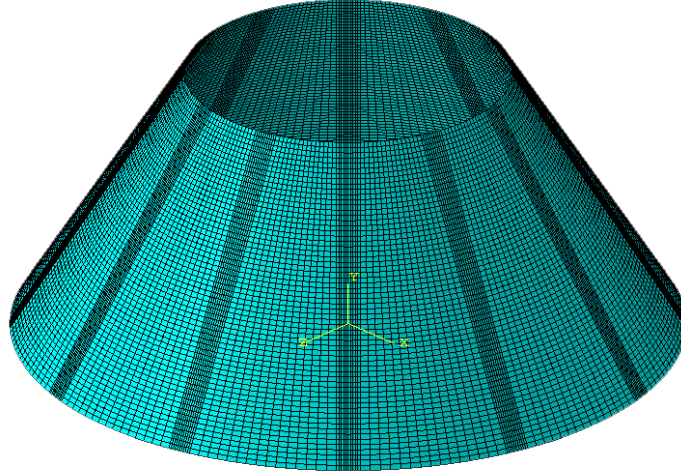
American Institute of Aeronautics and Astronautics

Figure 18. ABAQUS model of dual-matrix conical shell with free boundary conditions.

in Section IV.B.2, a frequency of 6.54 Hz is obtained. With a further ten-fold reduction of stiffness the natural frequencies are reduced by more than half, but are still above the 1 Hz frequency requirement.
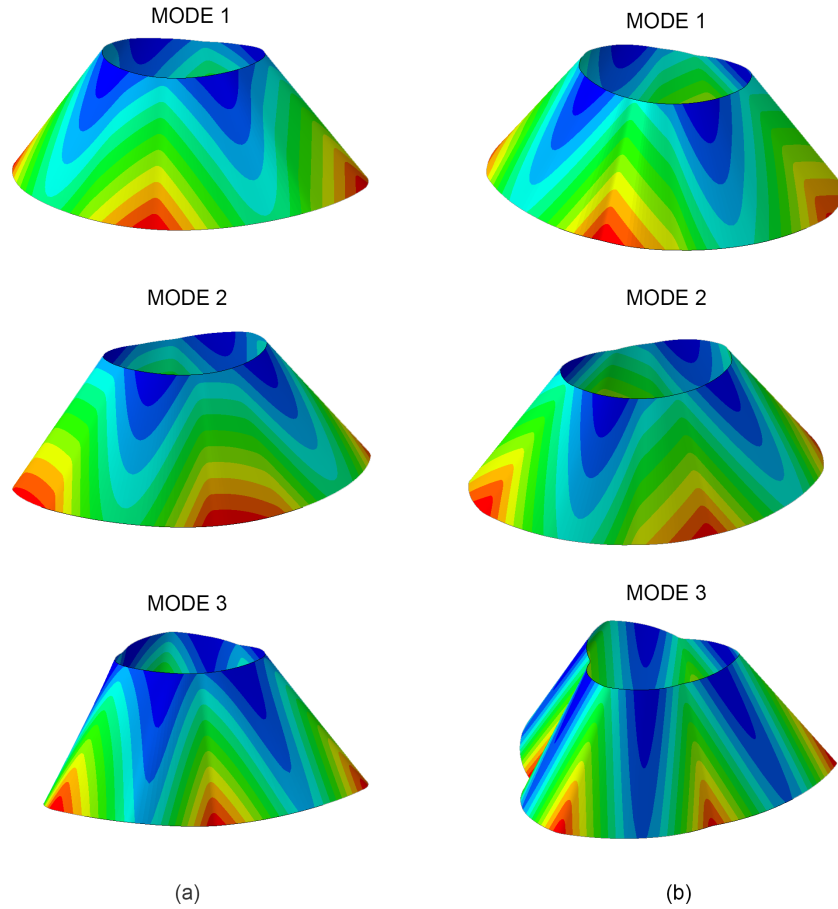

Figure 19. Mode shapes for the 3 first natural frequencies of the antenna. For (a), $D_{creases} = D_{silicone}$, and for (b), $D_{creases} = 0.1 D_{silicone}$.

These results have confirmed the validity of the proposed antenna concept and hence a physical prototype was fabricated and tested using the dimensions and layup described in this section.

V.   Fabrication Techniques

In this section, the fabrication of a foldable dual matrix antenna is described. The manufactured shell is a six-ply plain-weave fiberglass that can be flattened and z-folded. The folding lines are 10 mm wide and embedded in silicone matrix. The remainder of the shell is embedded in the stiffer epoxy matrix. The dimensions of the shell are the same as the prototype described in Section IV.A.

The manufacturing process is composed of the following steps:

1. The glass fabric is cut with the required geometry and fiber directions of each ply. It is recommended to use a box cutter and to apply pressure on the fabric near the cut to avoid distortion of the fibers.

2. The individual laminas are spread over a PTFE sheet to avoid any adhesion of epoxy or silicone to the working area.

3. A kapton template is laser cut and used to mask the silicone hinge areas. The template allows for 10 mm silicone hinge regions.

4. The epoxy film is placed over the dry fabric and template (Figure 20). The resin is transferred to the fabric through the application of heat. Generally, one layer of epoxy per lamina is needed.

Figure 20. Epoxy film placed over dry fabric. The kapton hinge mask is not shown.

5. The laminate is made by stacking the individual plies in the required direction. The epoxy protective layer of the last ply is kept in place to act as a mask during the curing of the silicone. The first three laminas are stacked, followed by the conductor mesh, cut to the correct log spiral shape (Figure 21). The top three laminas are stacked on top of the conductor.

6. The liquid silicone is applied to the folding lines (Figure 22). To ensure uniformity in the distribution of the silicone, the silicone-impregnated areas are pressed with a polyurethane foam swab. This results in a total volume fraction of fiber in silicone of $V_{f,s} = 30-40\%$. However, the fibers are more concentrated at the center of the hinge with a layer of silicone present on the shell surface. The fiber volume fraction in the epoxy matrix part is $V_{f,e} = 40$ to 50%.

7. The silicone is cured with a UV lamp for 1 min. The lamp used to cure the prototype is a Spectroline XX15A. This lamp radiates UV-A light (315 to 400 nm wavelength) with an intensity of 1.1 mW/cm^2 at a distance of 25 cm. The distance between the lamp and the shell is 4 cm, which results in an irradiance of approximately 40 mW/cm^2 With this exposure, the curing time is no more than one minute for the thickness of this laminate. The silicone that flows outside the folding lines does not cure, due to the masking of the UV light by the epoxy film that has not yet been removed. Having transferred the epoxy to the fabric before the silicone was applied prevents the silicone from spreading too far, as capillarity is reduced. Figure 23 shows the shell under the UV lamp during the curing of the silicone matrix.

American Institute of Aeronautics and Astronautics

Figure 21.   Conductor positioned over the first three plies of the laminate.
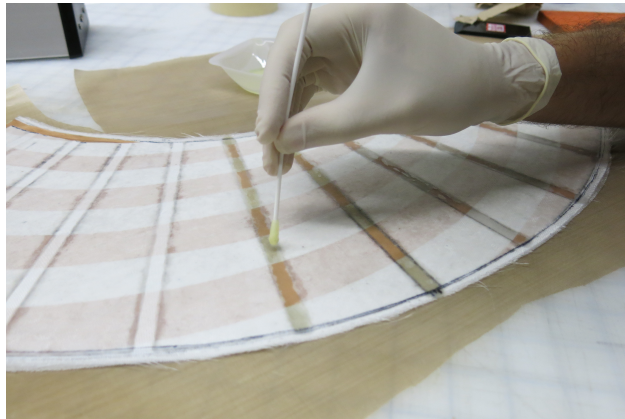

Figure 22.   Application of silicone to the hinge regions.
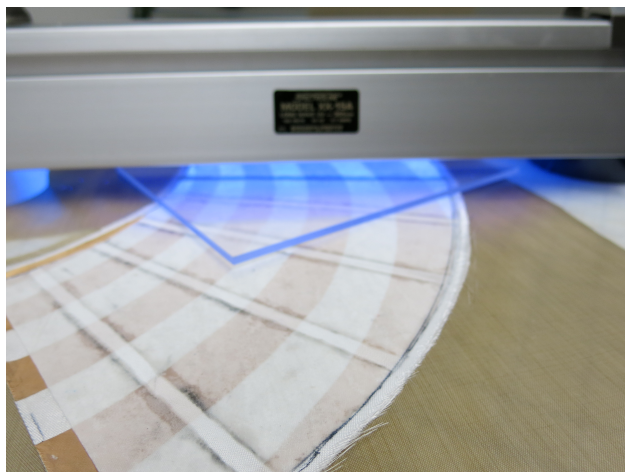

Figure 23.   UV curing of silicone. The epoxy film paper acts as a mask so that the silicone only cures in the exposed area. The curing time is less than one minute.

American Institute of Aeronautics and Astronautics

8. Once the silicone is fully cured, the epoxy protective film is removed from the shell. The shell is wrapped around a custom conical mold. A release film and a breather are placed on top of the shell. Then, a vacuum bag is placed and sealed with vacuum tape (Figure 24).

Figure 24. Antenna on custom mold with vacuum bag ready to be cured in autoclave.

9. The epoxy is cured in vacuum for one hour at 125 ^{o}C and 600 kPa.

The final prototype, after curing and removal from the mold can be seen in Figure 25.

Figure 25. Fabricated antenna prototype.

The shell manufactured with this process was folded into a compact configuration. Upon release the stored strain energy in the folding lines allows the shell to return to the original state when released. Figure 26 shows the shell in the original configuration, in its partially stowed state and in the fully compact configuration. No fiber failure was observed around the fold lines. The curvature radius of the folds was $\sim$ 1 to 2 mm.

American Institute of Aeronautics and Astronautics

Figure 26. Antenna folding process.

American Institute of Aeronautics and Astronautics

V.A.   Fabrication Process Alternative

The use of UV-cure silicone in the flexible fold lines limits the concept of dual-matrix composites to translucent glass fibers. However, for structural applications other than antennas, carbon fibers are better suited than glass fibers due to better mechanical properties and lower thermal expansion resulting in better dimensional stability. Furthermore, the use of two-component addition cure silicones is preferred to UV-cure silicone due to higher strain capabilities. Different from UV-cure systems which require radiation for cure, these silicones commonly cure at room temperature for 24 hours.

First attempts at manufacturing dual-matrix composite shells from glass fiber Astroquartz and the two-component addition cure silicone ELASTOSIL RT601 from Wacker showed that the silicone cure is inhibited when used next to the epoxy resin. As the glass fiber reinforced silicone cures normally when not in contact with epoxy resin, it is believed that the curing inhibition was caused by a chemical reaction between the epoxy, the silicone and the fiber sizing in the Astroquartz fabric. It was found that the fiber sizing can be removed by heating the dry Astroquartz plies at 500C for one hour prior to impregnation. This treatment allowed the use of the two-component silicones in glass fiber dual-matrix composites.

The use of these two-component silicones in the fabrication of Astroquartz dual-matrix composites requires no changes to steps 1 to 6 of the previous section. After impregnating the fold lines with the silicone, the cure of the dual-matrix composite shell can be carried out either in a serial or parallel fashion. In the serial cure approach, silicone and epoxy are cured separately, meaning that the silicone is cured first at room temperature for approximately 24 hours in the unfolded configuration of the shell. This cure should be carried out under the compressive load of a PTFE foil coated steel plate for increasing compaction and reducing laminate thickness in the reinforced silicone folds. Once the silicone is fully cured, the epoxy cure is performed according to steps 8 and 9.

As the cure time of addition cure silicones significantly decreases at elevated temperatures, these silicones can be co-cured with the epoxy at high temperature and pressure in the final shape of the conical shell, which greatly reduces processing time. In this parallel cure approach, the preform is wrapped around the conical mandrel after the fold lines have been impregnated with silicone and both matrix systems are cured together in the autoclave using the standard vacuum setup shown in Figure 24. Due to the shorter cure time of the silicone at higher temperatures (10 min. at 100C for ELASTOSIL RT601), both matrix systems are fully cured after the predetermined curing parameters of the epoxy resin (one hour at 125°C and 600kPa).

The parallel cure process had the advantage that higher fiber volume fractions can be achieved in the fold lines due to the high compaction pressure applied in the autoclave. Serial cure, on the other hand, results in lower fiber volume fraction as the silicone folds are cured under lower compression. For instance, dual-matrix composites made from four-ply T300-1K plain-weave carbon fiber showed fiber volume fractions in the reinforced silicone hinges of 50% for autoclave cure as opposed to 37% for room temperature cure. Bending tests performed on these single-hinged carbon dual-matrix composites showed that the bending stiffness of the reinforced silicone hinges increases with the fiber volume fraction, which is in agreement with the behavior of common fiber/epoxy composites. However, micrographs of these dual-matrix composites showed less matrix mixing when curing the silicone separately from the epoxy resin.

The fabrication of dual-matrix composite shells further showed that, when using reinforcement fabrics with greater areal weight than thin-ply Astroquartz, it becomes increasingly challenging to ensure uniformity of the silicone distribution throughout the fold lines when painting the silicone on top of the ply stacking (step 6). This runs the risk of non-uniform fiber volume fractions and increased matrix mixing. An improved method for impregnating the fold lines, which has been attempted in the fabrication of dual-matrix composite shells made from T300-1K plain-weave, is to apply the silicone to the dry fold line areas of each fabric before stacking the impregnated plies. This method provides better control of the amount of silicone applied to the hinge regions and hence achieves more uniform silicone distribution and fiber volume fractions throughout the hinge.

VI.   Structural Tests

A vibration test of the manufactured antenna prototype was conducted to verify the vibration frequency simulations and to confirm the value used for the out-of-plane bending stiffness of the hinges. The prototype was suspended using strings made of Spectra fibers to simulate free boundary conditions. The suspension resembled a double pendulum with string lengths adjusted such that the natural frequency of the suspension was well below the expected frequencies of the antenna. The chosen lengths were 32 cm for the upper string

and 12 cm for the lower string, resulting in a frequency of 1.5 Hz (less than lowest expected frequency of 2.5 Hz).

The excitation was provided by a Labworks Inc. ET-132 electromagnetic shaker. A sinusoidal sweep ranging from 3-30 Hz over 450 s was produced using an Agilent 33250A Waveform generator and was routed through a Labworks Inc. pa-138 power amplifier to the shaker. The shaker transmitted the excitation to the antenna using a 19.5 cm long stinger. The force applied to the antenna was measured using a PCB Piezotronics ICP 208C01 Force Sensor attached to the end of the stinger at one end and to the prototype using wax at the other end.

The output response of the antenna was measured by two laser displacement sensors. A Keyence LK G157 laser measured the displacement at the top of the prototype opposite the applied excitation, and a Keyence LK G087 laser measured the displacement at the bottom of the prototype. The displacements were measured at multiple points in order to capture the different vibration modes.

All analog input signals were wired as differential inputs into an NI USB 6210 data acquisition system and the data was collected and analyzed using the Mathworks Matlab software. See Figure 27 for a schematic of the experimental setup.
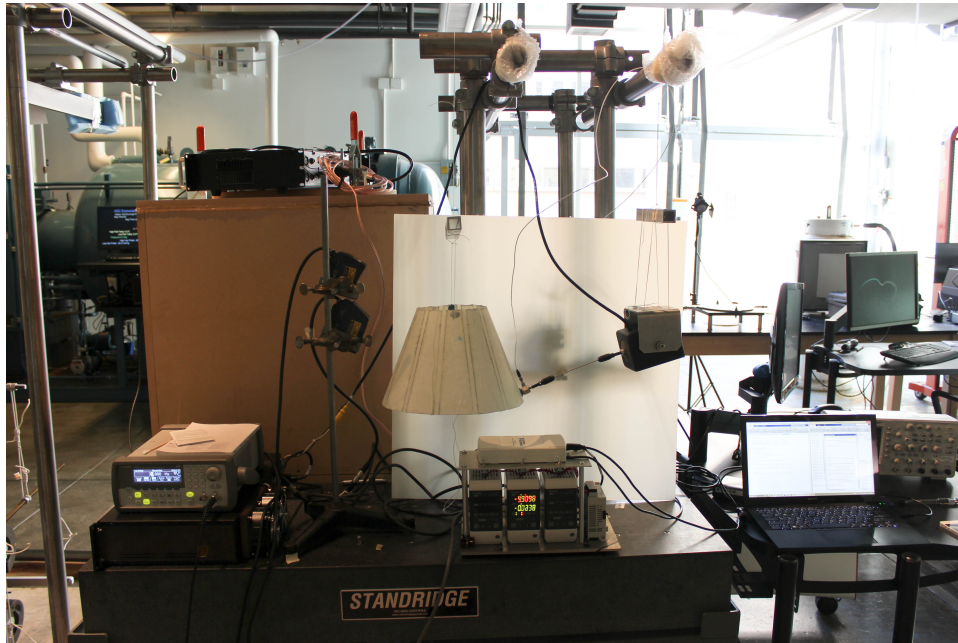

Figure 27. Experimental setup for vibration analysis.

The measured force and displacement signals were filtered using a high pass Butterworth filter (stopband frequency of 2.8 Hz, passband frequency of 3 Hz, stopband attenuation of 60 dB, and 1 dB of ripple allowed in the passband) to eliminate low frequency oscillations observed in the force sensor data. Welch's method was used to determine the power spectral density of each signal. In this scheme, the signal is divided into overlapping sections, each of which is windowed, and a discrete Fourier transform of each is performed. This method has the advantage of significantly reducing noise in the signal at the cost of reduced frequency resolution. Here, 30 sections with 50% overlap were used and a frequency resolution of 0.01 Hz was still achieved. The ratio of the displacement to the input force was used as a frequency response function to extract the natural frequencies of the system.[5]

The measured frequency response functions of the antenna prior to folding and after a folding-unfolding cycle are shown in Figures 28 and 29, respectively. The resulting natural frequencies are given in Table 5.

	f_1 (Hz)	f_2 (Hz)	f_3 (Hz)
Pre-folded Shell	8.21	12.02	25.84
Post-folded Shell	8.15	14.48	25.70

Table 5. First three natural frequency measurements.

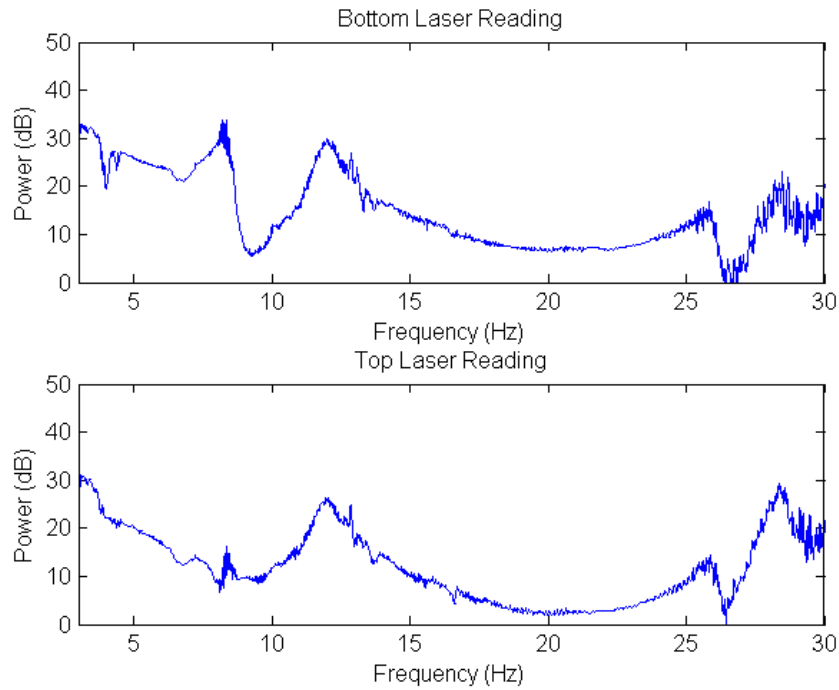American Institute of Aeronautics and Astronautics

Figure 28. Frequency response function of unfolded antenna analyzed using Welch's method.
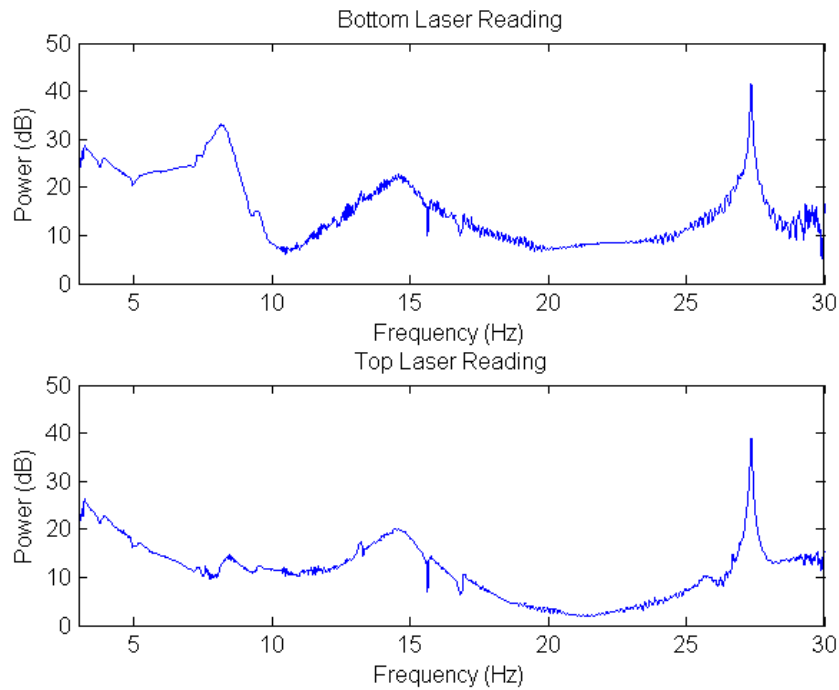

Figure 29. Frequency response function of folded antenna analyzed using Welch's method.

In order to compare to the simulation results, the ABAQUS model previously described was modified to account for the mass of the force sensor. Since the force sensor was attached directly to the antenna prototype it become part of the excited system and the frequencies measured were for a combination of the antenna and the force sensor. This effect was important since the sensor weight of 26 g was a significant portion of the antenna weight of 79 g. The force sensor was modeled as a rigid body and was added to the

American Institute of Aeronautics and Astronautics

simulation as a 26 g point mass at the bottom of the antenna using the *MASS command. The total mass of the simulated system was verified to match the combined mass of the physical system of 105 g.

	f_1 (Hz)	f_2 (Hz)	f_3 (Hz)
Pre-folded Shell	8.74	11.06	23.43
Post-folded Shell, 10% Stiffness	4.97	6.43	13.75

Table 6. First three natural frequency predictions from finite element simulations.

Table 6 shows the natural frequencies obtained using the modified simulations. The experimentally obtained frequencies agree with these simulations within 10 % for the pre-folded shell. Any discrepancies are likely due to the fabrication process which resulted in imperfections such as wrinkles in some layers of the laminate and a non-uniform thickness distribution. More importantly, the post-folding shell frequencies show little change from the pre-folded shell. It was noted that a folding and unfolding cycle results in very little residual curvature change of the shell. From Figure 17, it can be seen that for low curvatures the out-of-plane bending stiffness shows no change from the pre-folded hinges. As there is no change in the stiffness of the hinges, no corresponding change in natural frequencies is observed. The slight shift of the peaks of the frequency response function from the pre-fold to the post-fold configuration are likely due to further asymmetries introduced from folding the antenna manually.

The agreement between simulation and experiment indicates that the simulated natural frequencies given in Table 4 can accurately represent those of the free antenna. Moreover, no reduction in out-of-plane bending stiffness is required when simulating natural frequencies. As all frequencies are significantly above the required 1 Hz, resonance due to environmental forcing is not a concern for this design.

VII.   Electromagnetic Tests

The fabricated prototype was subjected to electromagnetic testing to verify the simulated performance. A vector network analyzer was used to measure the reflection coefficient of the antenna. The antenna's differential input impedance was designed to be 200 Ω. The feeding of the antenna was achieved using two 100 Ω coaxial cables connected to the output of a surface mountable balun. The coaxial cables were routed through the inside of the cone to reach the top of the conical log spiral antenna. Each cable was then directed to feed a conductor. A 50/200 Ω Anaren B0205F50200AHF balun was used to balance the signal into the two conducting arms of the conical antenna. The balun was soldered into a printed circuit that allows the input power to be divided equally among the two arms of the antenna, which achieving and impedance transformation from 50 Ω into a differential 200 Ω to feed the antenna accurately. The balun operation is between 150 - 680 MHz, which encompasses the expected antenna operating range. Figure 30 shows the deployed antenna connected to the feeding network.

The antenna's measured reflection coefficient is shown in Figure 31 in comparison with the balun's manufacturer's reflection coefficient. Using the standard cutoff of below -10 dB for the reflection coefficient, it can be seen that the antenna operates between 300 - 680 MHz. This shows good agreement with the simulated operating range of 318 MHz to above 600 MHz.

The measurement was repeated after the antenna was folded into its stowed configuration and deployed multiple times. Note that the feed inside the cone did not interfere with the folding of the antenna. No change in the antenna's frequency of operation was noticed with this measurement indicating that the folding of the antenna has no impact on antenna operation.

VIII.   Conclusion

A complete design-build-test cycle has been performed for a deployable conical log spiral antenna supported by a dual-matrix composite. Electromagnetic simulations were used to design a wideband, efficient antenna operating between 318 - 600 MHz, having a gain above 5 dB and circular polarization. A prototype made from Astroquartz fibers, an epoxy matrix for the stiff panels, and a UV cure silicone matrix for the soft hinges was fabricated. The prototype was subjected to structural and electromagnetic testing to verify simulated performance. Vibration tests showed that antenna natural frequencies are significantly higher than environmental forcing frequencies. Electromagnetic tests confirmed predicted wideband operation and high

American Institute of Aeronautics and Astronautics

Figure 30. Antenna deployed with feeding network connected.
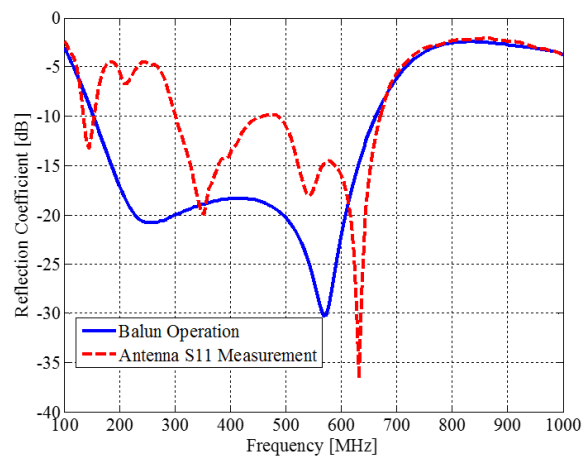
Figure 31. Comparison between reflection coefficients of the balun and the antenna.

American Institute of Aeronautics and Astronautics

gain of the antenna. Overall, this design iteration proved the feasibility of deployable dual-matrix antennas for CubeSats.

The design presented here can be extended to various folding schemes, including the efficient Miura-Ori pattern. Moreover, the dual-matrix composite concept is easily amenable to different antenna architectures. Future work will focus on a deployment concept for such antennas and the development of a general optimization strategy for the design of high-performance deployable antennas for small satellites.

Acknowledgments

References

[1] CAMPBELL, D., LAKE, M. S., AND MALLICK, K. A study of the bending mechanics of elastic memory composites. In *45th AIAA/ASME/ASCE/AHS/ASC Structures, Structural Dynamics, and Materials Conference, Palm Springs, CA* (2004), American Institute of Aeronautics and Astronautics.

[2] DANIEL, I. M., AND ISHAI, O. *Engineering mechanics of composite materials*. Oxford, 1994, second edition.

[3] DATASHVILI, L., BAIER, H., WEHRLE, E., T, K., AND HOFFMANN, J. Large shell-membrane space reflectors. In *51st AIAA/ASME/ASCE/AHS/ASC Structures, Structural Dynamics, and Materials Con- ference, Orlando, Florida* (2010), American Institute of Aeronautics and Astronautics.

[4] DYSON, J. The characteristics and design of the conical log-spiral antenna. *IEEE Transactions on Antennas and Propagation 13* (1965), 488–499.

[5] EWINS, D. J. *Modal Testing: Theory, Practice, and Application*. Research Studies Press Ltd, second edition, 2000.

[6] FISCHER-CRIPPS, A. C. *Nanoindentation*. Springer, third edition, 2011.

[7] LOCTITE. Loctite 5055. `https://tds.us.henkel.com/NA/UT/HNAUTTDS.nsf/web/88C664FFAF9001438525775E006CE0B0/ $File/5055-EN.pdf`. Accessed: 3–14–2013.

[8] LOPEZ JIMENEZ, F., AND PELLEGRINO, S. Folding of fiber composites with a hyperelastic matrix. *International Journal of Solids and Structures 49*, 3/4 (2012), 395–407.

[9] LOPEZ JIMENEZ, F., AND PELLEGRINO, S. Failure of carbon fibers at a crease in a fiber-reinforces silicone sheet. *Journal of Applied Mechanics 80* (2013).

[10] MAQUEDA, I., PELLEGRINO, S., AND MEJIA-ARIZA, J. M. Characterization of a high strain composite material. In *53st AIAA/ASME/ASCE/AHS/ASC Structures, Structural Dynamics, and Materials Conference* (2012), American Institute for Aeronautics and Astronautics.

[11] MEJIA-ARIZA, J. M., GUIDANEAN, K, MURPHEY, T. M., AND BISKNER, A. Mechanical characterization of l'garde elastomeric resin composite materials. In *51st AIAA/ASME/ASCE/AHS/ASC Structures, Structural Dynamics, and Materials Conference, Orlando, Florida* (2010), American Institute of Aeronautics and Astronautics.

[12] MURPHEY, T. W., MEINK, T., AND MIKULAS, M. M. Some micromechanics considerations of the folding of rigidizable composite material. In *42nd AIAA/ASME/ASCE/AHS/ASC Structures, Structural Dynamics, and Materials Conference, Seattle, WA* (2001), American Institute of Aeronautics and Astronautics.

[13] OLSON, G. M., PELLEGRINO, S., COSTANTINE, J., AND BANIK, J. Structural architectures for a deployable wideband uhf antenna. In *53rd AIAA/ASME/ASCE/AHS/ASC Structures, Structural Dynamics and Materials Conference, 23-26 April 2012 Honolulu* (2012), American Institute of Aeronautics and Astronautics.

[14] SAITO, K., PELLEGRINO, S., AND NOJIMA, T. Manufacture of arbitrary cross-section composite honeycomb cores based on origami techniques. In *Proceedings of the ASME 2013 IDETC/CIE, Portland, Oregon* (2013), American Society of Mechanical Engineering.

[15] SOYKASAP, O. Micromechanical models for bending behavior of woven composites. *Journal of Spacecraft and Rockets 43*, 5 (2006), 1093–1100.

[16] TODOROKI, A., KUMAGAI, K., AND MATSUZAKI, R. Self-deployable space structures using partially flexible cfrp with sma wires. *Journal of Intelligent Material Systems and Structures 20* (2009), 1415–1424.